Improve the dielectric properties of PrSrNi0.8Mn0.2O4 compounds by longer mechanical milling

A. Chouket, O. Bidault, L. Combemale, O. Heintz, M. Khitouni, V. Optasanu

This is a working paper and could be slightly different from the final paper. The final paper is available here: https://doi.org/10.1016/j.jallcom.2017.10.098

Improve the dielectric properties of $PrSrNi_{0.8}Mn_{0.2}O_4$ compounds by longer mechanical milling

A. Chouket[1], O. Bidault[1], L. Combemale[1], O. Heintz[1], M. Khitouni[2], V. Optasanu[1*]

1. Laboratoire Interdisciplinaire Carnot de Bourgogne (ICB), UMR 6303 CNRS-Université de Bourgogne 9, AV. Alain Savary BP 47870, 21078 DIJON Cedex, France.
2. Laboratoire de Chimie Inorganique, Ur-11-Es-73, Faculté des Science de Sfax, BP 1171, Université de Sfax, 3018 Sfax, Tunisia.

Abstract :

Structural and dielectric properties of $PrSrNi_{0.8}Mn_{0.2}O_4$ ceramics elaborated by a rapid method combining mechanical milling and heat treatment were studied for the first time. The raw materials are milled at different times (t_{mil} =0, 5, 10, 20 and 30 hours) and annealed at 1300°C for 8 hours to produce a revealed $PrSrNi_{0.8}Mn_{0.2}O_4$ single phase, exhibiting tetragonal structure with space group I4/mmm. This result was confirmed by using the TEM/ED pattern for sample milled at 30 h using the [001] orientation. The corresponding lattice images show a well-ordered compound, indicating the absence of stacking faults and the growth of the crystallites. Giant dielectric response was observed in these ceramics, and only one dielectric relaxation was found on the curve of a dielectric constant as a function of the temperature. The dielectric loss drops with increasing milling time. For 30 h milling it is divided by 100 at room temperature for low frequencies compared with 5 h milling. An equivalent circuit [R-C][R-CPE] was used to fit the experimental data and provide the activation energy of the thermally activated relaxation. Using the same nominal composition, the milling time has a major effect on the dielectric constant by significantly reducing the losses.

Keywords: Mechanical milling method; microstructure; K_2NiF_4-type structure; XRD Rietveld refinement; Impedance spectroscopy; Equivalent circuit.

1. Introduction

After the discovery of temperature-stable giant dielectric constant in $CaCu_3Ti_4O_{12}$ (CCTO), compounds with giant dielectric constants (GDC) received scientific attention for their potential application in the field of microelectronics [**1-6**]. The electrode/ceramic interface and grain boundary play a major role in the giant dielectric response of $CaCu_3Ti_4O_{12}$. The value of the dielectric constant measured in mono-crystalline $CaCu_3Ti_4O_{12}$, which is close to the poly-crystalline ceramics value, shows that the giant dielectric response should also have other origins [**7,8**]. Among these materials, the nickelates with K_2NiF_4 structures are highlighted because of their temperature-stable giant dielectric responses at high frequencies. Considerable dielectric response can be measured up to gigahertzes at room temperature [**9,10**]. In the particular case of $Ln_{1.5}Sr_{0.5}NiO_4$ceramic (Ln = La, Nd and Sm) authors [**11,12**] have measured GDR up to high frequencies. The most promising dielectric properties were observed in $Sm_{1.5}Sr_{0.5}NiO_4$ ceramics, where the dielectric constant is about 10^5 at high frequency (5 MHz) and the dielectric loss about 10^{-1}. The Nickelates system has been well received by industry in recent years. This is due to their enormous dielectric permittivity. These compounds are used worldwide in advanced technology. The observation of unusual, high dielectric loss (tanδ) at room temperature has focused attention on the possible reasons for this behaviour, with the objective to understand the mechanism and, ultimately, to reduce that loss. A large effort was devoted to the suppression of electrical conductivity induced by using Mn-substitution in transition-metal oxides. Li et al. [**13**] have reported the decrease of bulk conductivity in Mn-doped CCTO. Qin et al. [**14**] have reported that the introduction of Mn ions into $Lu_2Fe_2Fe_{1-x}Mn_xO_7$ can efficiently suppress the electrical conducting leakage. After analysing the relationship between the electrical resistivity and

Mn^{3+} content in $La_{0.7}Ca_{0.3}MnO_{3-\delta}$ thin films, Teresa et al.[**15**] found that the polaron binding-energy is proportional to the Mn-O octahedral distortion.

There are several preparation methods for obtaining the compounds that interest us. However, the condition and the preparation method are closely associated with the extrinsic properties of materials and can greatly affect their physical properties, especially the character of the electrical transport. In recent years, the mechanical alloying method has been used for various kinds of materials, such as alloys or mixed oxides (ABO_3). To the best of our knowledge, we are the first authors to use this method to elaborate oxides derived from K_2NiF_4 perovskite-type. High-energy ball milling [**16, 17**] is a very popular technique thanks to the low-cost, high efficiency and low temperature synthesis it offers. This method was extensively used for the synthesis of rare-earth permanent magnets and intermetallic compounds [**18, 19**]. Also, the mechanical ball milling technique is an important method in powder metallurgy because of its high flexibility, simple control of process parameters, and ability to produce a wide range of materials with fine particles. Moreover, mechanical ball milling technique has also been used to produce commercially important alloys, particularly those with a very high melting point [**20**]. Synthesis of these materials has been extensively studied using different routes, but the mechano-chemical method itself (used not only as activation technique) is not yet common [**21**]. Mechano-chemistry is a relative simple process that uses high-energy ball mills and permits production of nanostructured mixed oxides [**22**]. The mechanical energy coming from impact and shear forces by application of a high frequency movement is transferred to the powder, inducing solid state chemical reactions. One of the most important advantages of mechano-chemistry is its ability to produce large quantities of material at room temperature and in a relatively short time. Previously, we worked on dielectric and microstructure characterization on $LaSrNi_{1-x}Mn_xO_4$ ceramics obtained by high-energy mechanical milling method [**23, 24**]. We revealed a large dielectric

constant ~10^5 at room temperature but a modest dielectric loss, showing that for potential applications this compound has to be modified in order to optimize its properties. In a previous work [**25**] we substitute Ni by Al in $La_{1.6}Sr_{0.4}NiO_4$ compound elaborated by the Pechini method and then generate a remarkable variation of the dielectric properties. However, the measured dielectric losses show that this compound still needs to be optimized. These promising results encouraged us to continue the optimisation of the dielectric properties of this family of compounds by taking advantage of the super-exchange and double-exchange interactions between Ni^{2+}/Ni^{3+} and Mn^{3+}/Mn^{4+} ions when the material is synthesized by high-energy ball milling. In order to understand the effect of milling time on the structural and physical properties, as well as on the dielectric properties, the compound $PrSrNi_{0.8}Mn_{0.2}O_4$ was prepared using various process durations.

In this work, we introduce the high-energy ball milling method to synthesize the $PrSrNi_{0.8}Mn_{0.2}O_4$ layered perovskite and then discuss optimal milling efficiency. We also investigate the structural properties of the as-milled powders. The structural and dielectric characteristics of the samples were studied after high-temperature sintering.

2. Experimental procedures

MnO_2 (purity >99.9%, Particle size <10 μm), Pr_6O_{11} (purity >99.9%, Particle size <0.2 μm) NiO (purity >99.9%, particle size <44 μm) and SrO powders were used as raw materials. The last one was obtained from calcination of $SrCO_3$ (Aldrich 98%, Particle size 1–2 μm)) at 1200 °C for 12 h. The possible chemical reaction is given by Eq. (1):

$$1/6Pr_6O_{11} + SrO + 0.8NiO + 0.2MnO_2 \rightarrow PrSrNi_{0.8}Mn_{0.2}O_{4\pm\delta} \qquad (1)$$

These oxides were mixed with respect to the molar ratio of cations. The powder mixture was mechanically activated using a planetary ball mill (model Micro-Mill Pulverisette 7, Fritsch). The powder-to ball weight ratio and the rotational speed were 5:1 and

600 rpm, respectively. To prevent the heating and sticking of the powder to the container walls and balls, as well as powder agglomeration during the process, the milling sequence was 10 min of milling followed by a 5 min stop period. Milling was conducted in the ambient atmosphere for 5, 10, 20 and 30 h milling. 1 g of each milled sample was then uniaxially pressed into pellets of 12×5 mm at room temperature and sintered in air at 1300 °C for 8 h with a heating rate of 10 °C min^{-1} and free cooling. The structural changes of the milled samples were investigated by X-ray diffraction (XRD) by means of a Bruker D8 Advance diffractometer in a (2θ) geometry using CuK_{α} radiation (λ = 0.15406 nm). The microstructural parameters were taken out from the refinement of the XRD patterns by using the MAUD program [**26**], which is based on the Rietveld method.

The phase purity of the samples after sintering was confirmed by X-ray powder diffraction. The XRD patterns were collected in the range of 10–90° with a step size of 0.05°. The structure was analysed by Rietveld method using the FullProf program, and a pseudo-Voigt profile function with preferred orientation correction [**27, 28**]. X-Ray photoelectron spectroscopy analysis was done using PHI Versaprobe 5000 apparatus with $AlK_{\alpha 1}$ monochromated line (energy of 1486.7 eV, power of 50 W and X-Ray spot diameter of 200 μm). The C1s peak from pollution (at 284.8 eV) was considered for the energy calibration. During measurements, the residual pressure of the analysis chamber was maintained below 10^{-7} Pa. Spectra were treated with the Casa software package. The microstructure was studied by transmission electron microscope (TEM) at room temperature and the stoechiometric ratio was detected by energy dispersive X-ray spectroscopy (EDS). The dielectric properties of these ceramics were investigated with a dielectric spectrometer (HP 4284) over a wide range of temperatures (80–450 K) and frequencies (100 Hz–1 MHz) with a heating rate of 1 $K.min^{-1}$. Sputtered platinum was used as electrodes.

3. Results and discussion

3.1. Milled powder before sintering

Figure 1 presents the XRD patterns showing the evolution of the crystalline structure of the powder for 5, 10, 20 and 30 h milling. The X-ray pattern of the unmilled powder mixture is also presented in the same figure for comparison. Before milling, the recorded peaks correspond to the free oxides Pr_6O_{11} [**29**], SrO [**30**], MnO_2 [**31**] and NiO [**32**]. The vanishing and/or the appearance of some peaks can be assigned to the mixing of the elemental powders and, therefore, to the formation of new solid solutions [**33**]. After 5 h of milling, the peaks corresponding to the initial oxides became asymmetric and started to broaden. Further, one can see that peaks (2θ=29.04°) and (2θ=77.4° and 79.7) corresponding respectively, to SrO and MnO_2 oxides, completely disappear (Fig. $2b_1$ and b_2). These observations demonstrate that SrO and MnO_2 gradually reacted with Pr_6O_{11} and NiO, respectively, to form the $(Pr,Sr)_6O_{11}$ (Space group $P2_1/c$, a=6.6780(2) Å , b=11.6124 (4) Å , c=12.8191(4) Å , β= 51.432(2)°, 99.964(1)°) and (Ni,Mn)O (Space group Fm-3m, a= 4.2158(1) Å) solid solutions. Extended milling to up to 10 h led to the formation of $PrNiO_3$ phase (space group: Pbnm, a=5.465(1) Å, b=5.4429 (4) Å, c=7.6277(4) Å solid solution (Fig.$2c_1$ and $2c_2$). After 20 h, the formation of $PrNiO_3$ occurred in significant quantities (Fig.$2d_1$ and $2d_2$). The complete disappearance of precursor's diffraction peaks above this milling time would appear to be due to completion of the oxides' solid solution formation. For extended milling times (up to 30 h milling), identical solid solutions were identified. Also one can notice that all the diffraction peaks broaden, indicating a decrease of the crystallite size and the introduction of lattice strains. The dependence of the calculated average crystallite size and microstrains on milling time of as-milled powders is given in Fig. 3. In the initial state the crystallites size is about 250 nm. It becomes less than 50 ± 2nm after 20 h of milling. After that, the mean value of crystallite size remains nearly constant. The lattice strains increase with the milling time to an

average value of about 0.56 % after 5 h. Further, they show a slight decrease followed by a continuous increase at extended milling time to reach 0.65 % after 30 h. The crystallite size refinement and high density of defects could also be caused by the reaction between raw materials. In fact, since nanocrystalline materials contain a very large fraction of atoms at the grain boundaries, the numerous interfaces provide a high density of short circuit diffusion paths, thus allowing them to exhibit enhanced diffusivity.

3.2. Sintered compounds

The results of XRD given in Fig. 1 show that a reactive sintering process is necessary in order to obtain the desired phase. After sintering at 1300°C in air for 8 h, the room-temperature XRD analysis showed that all samples were single-phase crystallized in the tetragonal lattice with I4/mmm space group and no detectable impurities (Fig. 4). As an example, Fig. 5 depicts the Rietveld refinement for the sample milled for 30 h. Table 1 summarizes the structural parameters obtained by Rietveld analysis of the diffraction patterns using FullProof program. One can observe that as the milling time increases the most intense diffraction peak shifts to low angles (see inset in Fig. 4). This result indicates an increase of the unit cell with milling time, showing a slight increase of interatomic distances. The average crystallite size was calculated based on the most intense peak using Scherrer's formula [**34**] :

$$D_{sc} = \frac{K\lambda}{\beta cos\theta} \qquad (2)$$

where K is a constant close to 0.9, λ is the wavelength of the incident X-ray, θ is the diffraction angle, and β is the full-width at half maximum. The values obtained for the crystallite size (D_{SC}) are 76, 69, 61 and 53 nm for samples milled for 5, 10, 20, and 30 h, respectively. One can conclude that the increase of the milling time clearly leads to the reduction of the crystallites size.

Figure 6 shows the evolution of the parameters a and c and the volume of the unit cell for all compounds. Both a and c lattice parameters change with the milling time. The unit cell volume increases with increasing milling times, as illustrated in Table 1. As the chemical composition is the same, this may reflect a small change of the oxygen content and/or the cationic oxidation degree (Pr^{2+}/Pr^{3+}, Ni^{2+}/Ni^{3+} and $Mn^{2+}/Mn^{3+}/Mn^{4+}$). Then, one have to point out that, even after the sintering treatment step, the effect of the milling time on the microstructure persists: the lattice parameters, the unit cell volume and the crystallites size show a monotone evolution.

In order to determine whether the milling process produces modifications of the chemical environment, XPS measurements have been carried out. Those measurements also make it possible to determine if the milling process induces any contamination of the samples. The planetary milling device and balls are made of stainless steel. The XPS spectrum obtained on the powders milled for 30 h is shown in Fig. 7. As remarked, no traces of pollutants (iron and/or chromium) can be detected. Thus, the powders do not seem to be contaminated by the milling device (as far as the XPS precision can reveal). To examine the changes in the samples' composition the powders milled at different times were investigated by XPS. Figure 8 show the peaks of the XPS spectrum for the main chemical elements of the samples: Pr, Sr and Ni. Using the $K_{\alpha 1}$ line of aluminum for excitation, nickel Auger transitions and manganese 2p levels are found at very close energies. Thus, under our experimental conditions, and considering the expected low concentrations of manganese, the 2p levels of Mn are not detectable. As depicted in Fig. 8a and b, the curves corresponding to Pr 3d, and Ni 2p do not change during the milling and thus no evolution of the chemical environment is observed. On the other hand, for strontium, a slight displacement of the 3d levels is observed towards the highest binding energies (Figure 8c and 8d). This can be interpreted as an effect of the enrichment of oxygen concentration in the vicinity of Sr.

TEM and ED analysis were also used to characterize the structure, microstructure and the purity of the milled sample for 30 h. The results are given in Fig.9. The electron diffraction patterns of $PrSrNi_{0.8}Mn_{0.2}O_4$ were recorded from several crystallites, and they all show the same shape. The brighter reflections on the ED patterns correspond to the tetragonal lattice structure along [001] zone axes. The ED pattern for samples using the [001] orientation was successfully indexed on the basis of the tetragonal unit cell with space group I4/mmm (Fig. 9a). This data confirms the result established by XRD. The [001] zone does not show any indication of the $\sqrt{2}a \times \sqrt{2}a$ cell, which would result from B site cation ordering. The corresponding lattice image shows a nearly ordered structure, indicating the presence of a low density of stacking faults. Several TEM images were recorded, showing that the size of the powder grains is inhomogeneous, varying between 20 and 100 nm. The TEM micrograph presented in fig. 9b shows a grain of about 50 nm. Further, the HRTEM micrograph show a crystal oriented along the [001] axis with a tetragonal structure (Figure 9c). The EDX analysis result shown in Fig. 9d reveals that the powders are composed of only Pr, Sr, Ni, Mn and O elements with atomic percent values of 15.10, 15.27, 10.86, 2.73 and 55.97, respectively. This matches closely the nominal composition of the powder mixture.

Dielectric constant measurements were made in order to study the properties of $PrSrNi_{0.8}Mn_{0.2}O_4$ sample milled at different times followed by a heat treatment. Figure 10a depicts the real part of the dielectric constant, ε', recorded at 293 K between 1 kHz and 1 MHz for three different samples milled for 5, 10 and 30 h. The high value observed for sample milled for 30 h (around 10^5 at 1 kHz) gradually decreases as the milling time decreases. The shape of ε'(ω) curve suggest a Debye relaxation phenomenon. Moreover, the relaxation frequency shifts to a lower value as the milling time increases. The evolution of the dielectric parameters show that the relaxation is highly sensitive to the milling time. As shown in Fig. 10b, the dielectric losses are relatively high, especially in the low frequencies region.

Moreover, the dielectric loss decreases with increasing milling time: at low frequency (10^3 Hz), the value of the loss is greatly reduced (divided by two orders of magnitude) at room temperature when the milling time increases from 5 to 30 h. It is well known that the increase of milling time favours high density of structure defects, and this may enhance the dielectric response. As a conclusion, extended milling time produces the increase of the dielectric constant and the decrease of the dielectric loss. The increase of the dielectric constant value may be may be related to a bigger ion disorder a higher internal stress and a smaller crystallite size given by the long milling process.

In the same way, we observed that the relaxation frequency shifts to lower values as the milling time increases. This phenomenon can mainly be attributed to the crystallite size decrease (see Table 1). According to the internal barrier layer capacitor model demonstrated by Adams et al. [**35**], based on the electrical heterogeneous behavior of CCTO, the values of the dielectric losses decrease by decreasing the crystallite size because the lower the crystallite size the higher the number of series grain boundary capacitors. This behavior has been checked in a number of papers [**36-38**]. Another probable reason for the relaxation shift is the changes in the chemical environment of the Sr, as shown by the XPS analyses.

Figure 11 shows the real part of the dielectric constant and the losses curves as a function of the temperature in the interval range of 100 - 450 K. As shown, a giant dielectric response was observed in all the samples ($\varepsilon' \sim 10^5$). In the temperature range considered here we can clearly see one dielectric relaxation, which leads to a giant dielectric constant plateau. The dielectric constant increases sharply at low temperature accompanied by a peak in the dielectric loss. As shown, the position of the peaks shifts to high temperature as the measuring frequency increases. This behaviour indicates the presence of thermally activated relaxations. The value of the dielectric constant becomes more and more stable as the milling time increases up to 30 h.

To investigate further the origin of giant dielectric response in different samples, the frequency dependence of dielectric constant at various temperatures was measured. The results are shown in the left part of Fig. 12. It is clear that the all samples exhibit considerable high dielectric constant at low frequency for the full range of temperatures investigated. The dielectric constant decreases slightly with increasing frequency and then drops noticeably at frequencies above 10 kHz. The dropping frequency decreases with the decreasing temperature. The active polarization mechanism can be employed to explain the dielectric constant decreasing with increasing frequency: at low frequencies, the dipoles can follow the alternating electric field, giving a higher value for the dielectric constant [**39**]. To inspect the lower frequency dielectric relaxation, the poly-dispersion modified Debye equation is used to fit the ε' − f curves:

$$\varepsilon^*(\omega) = \varepsilon' - i\varepsilon'' = \varepsilon_\infty + \frac{\varepsilon_S - \varepsilon_\infty}{1+(i\omega\tau)^{1-\alpha}} \qquad (3)$$

where (ε_s-ε_∞) is the amplitude of the relaxation, ε_s is the static dielectric constant, ε_∞ is the dielectric constant at very high frequencies, ω is the angular frequency, τ is the mean relaxation time and α represents the distribution degree of the relaxation time τ. The fitting curves are presented as solid lines in the left part of Fig. 12. The right part of Fig. 12 shows the dependence of the relaxation time on the reciprocal temperature. It follows the Arrhenius law:

$$\tau = \tau_0 \exp(\frac{E_a}{K_B T}) \qquad (4)$$

where E_a is the activation energy, τ_0 represents the relaxation time at very high temperature, k_B is the Boltzmann constant, and T is the absolute temperature.

The estimated values of E_a are respectively 29(4), 47(3) and 77(7) meV for 5, 10 and 30 h milling. The respective relaxation times at infinite temperature (τ_0) are 4.24 10^{-6}, 1.24 10^{-6} and 1.21 10^{-7} s. One can remark that the E_a value increases while the τ_0 value decreases with milling time.

To find the relationship between the dielectric relaxation and electrical conduction, the bulk and grain boundary resistance must first be identified. Iguchi [**40**] has shown that the impedance spectrum can be used to determine the contribution from the grain volume, grain boundary, and electrode/sample interface. The resistance values of the different elements of the circuit can be obtained from the real axis intercepts. The typical impedance spectra for $PrSrNi_{0.8}Mn_{0.2}O_4$ ceramics milled at two different times (10 and 30 h milling) at various temperatures were simulated with the EIS Spectrum Analyser software [**41**] using a [R-C][R-CPE] circuit. The experimental and simulated results are shown in Fig. 13. The arc produced at high frequency can be attributed to the grain volume, while the intermediate frequency arc is due to the grain boundary. In the present case, the response of the electrode/sample interface should be outside the frequency range. Using two connected arcs, the least-mean-square linear regressions are shown as solid lines in the plots of the right part of Fig. 13. The right-side intercept of the high-frequency arc is the resistance of the bulk, while that of the intermediate frequency arc is the total resistances of the bulk and grain boundary. The resistances of the bulk and grain boundary of the examined ceramics at different temperatures are obtained from the above analyses and the values are shown as symbols in Fig. 13. The adiabatic small polaronic hopping model is used to fit the extracted data [**11,12,42**]:

$$R = R_0 T^{\alpha} \exp\left(\frac{E_a}{K_B T}\right) \qquad (5)$$

where R_0 is constant related to the polaron concentration and diffusion, E_a is the polaronic hopping energy, and $\alpha = 1$ for the adiabatic case. The linear relationship between the natural

logarithms of R/T value and the reciprocal of temperature is observed in the temperature range of 90–300 K. The activation energies of grain boundaries and ceramic bulks are calculated using Eq. (5). The estimated values of E_a are 52(5), 73(8) meV for bulk powders milled for 10 and 30 h, respectively. The calculated E_a values for the grain boundary are 62(2) and 79(7) meV. The value of E_a for bulk is nearly equal to that of the dielectric relaxation mentioned above. These results show the correlation between dielectric relaxation and adiabatic small polaronic hopping process. The giant dielectric response of the present ceramics should be attributed to the polaronic hopping process. Moreover, the experimental results suggest that the dielectric response should be mainly attributed to the small polaronic hopping process, and so the response should be directly linked to the polaronic properties. The polaronic concentration should decrease with increasing milling times, while the polaronic size increases. The first parameter should induce a decrease of the conductivity (as well of the dielectric losses), while the second one is responsible for the enhancement of dielectric permittivity.

4. Conclusion

$PrSrNi_{0.8}Mn_{0.2}O_4$ oxide was successfully synthesized by the use of high-energy mechanical milling for different times (5, 10, 20 and 30 h) and heat treatment at 1300 °C for 8 h. The final product was identified as a ceramic single-phase with tetragonal structure.

The ED pattern for sample using the [001] orientation was successfully indexed on the basis of the tetragonal unit cell. The HRTEM analysis reveals some crystal domains with average sizes nearly 0.3 μm. Dielectric measurements of the $PrSrNi_{0.8}Mn_{0.2}O_4$in the temperature range 100 – 450 K revealed a giant dielectric constant ($\varepsilon' \sim 10^5$) and low dielectric loss. The very high values of the dielectric constant at room temperature make the material potentially attractive for applications. A peak was found on the dielectric loss curve. In addition, one

dielectric relaxation peak was found. The poly-dispersive Debye equation was used to fit the ε' - f curves and allows one to obtain the activation energy for the relaxation time. The simulation of the equivalent circuit impedance, according to the small polaronic model, allowed calculation of the activation energy for bulk and grain boundary. The comparison of the activation energy of these two models revealed that the low-temperature high-frequency dielectric relaxation of this sample can be attributed to the adiabatic small polaron hopping process.

By increasing the milling time, the relaxation parameters can be adjusted (amplitude and relaxation frequency). It appears that increasing the milling time (t_{mil}) produces not only significant reduction of the conductivity but also increases the dielectric relaxation amplitude as a consequence of the lattice volume increase.

The XPS analyses show that there is no detectable pollution of the powder during the milling process.

As a conclusion, for $PrSrNi_{0.8}Mn_{0.2}O_4$ ceramics, increasing milling time enhances the dielectric properties by producing very interesting high dielectric constant and small dielectric loss. The most promising dielectric response is given by the sample milled for 30 hours. These interesting results may probably be improved by longer milling times.

The main conclusion of this paper is that, for the same chemical composition of the material (with giant dielectric response), the increasing of the milling time produces an increase of the dielectric constant and a decrease of the dielectric loss. We believe that the structural modifications produced by the mechanical treatment before the sintering step are the main factors responsible for the dielectric parameters modification.

The milling conditions can be used as adjustable parameters to obtain the desired dielectric properties.

Acknowledgements

The authors thank to Conseil Régional Bourgogne Franche Comté and FEDER for the grant number E132.

References

[1] M. A. Subramanian, D. Li, N. Duan, B. A. Reisner, A. W. Sleight, J. Solid State Chem., 2000, **151**, 323.

[2] C. C. Homes, T. Vogt, S. M. Shapiro, S. Wakimoto, A. P. Ramirez, Science, 2001, **293**, 673.

[3] J. Wu, C. W. Nan, Y. Lin, Y. Deng, Phys. Rev. Lett., 2002, **89**, 217601.

[4] L. Ni, X. M. Chen, Solid States Com., 2009, **149**, 379.

[5] I. P. Raevski, S. A. Prosandeev, A. S. Bogatin, M. A. Malitskaya, L. Jastrabik, J. Appl. Phys., 2003, **93**, 4130.

[6] S. Krohns, P. Lunkenheimer, C. Kant, A.V. Pronin, H.B. Brom, A.A. Nugroho, M. Diantoro, A. Loidl, Appl. Phys. Lett., 2009, **94**, 122903.

[7] S. Krohns, P. Lunkenheimer, S. G. Ebbinghaus, A. Loidl, J. Appl. Phys., 2008, **103**, 084107.

[8] D. S. Fu, H. Taniguchi, T. Taniyama, M. Itohand, S-Y. Koshihara, Chem. Mater., 2008, **20**, 1694.

[9] S. Krohns, P. Lunkenheimer, Ch. Kant, A. V. Pronin, H. B. Brom, A. A. Nugroho, M. Diantoro, A. Loidl, Appl. Phys. Lett., 2009, **94**, 122903.

[10] P. Lunkenheimer, S. Krohns, S. Riegg, S.G. Ebbinghaus, A. Rellerand A. Loidl, Eur. Phys. J. Spec. Top., 2010, **180**, 61.

[11] X. Q. Liu, S. Y. Wu, X. M. Chen, H. Y. Zhu, J. Appl. Phys., 2008, **104**, 4114.

[12] X. Q. Liu, Y. J. Wu, X. M. Chen, H. Y. Zhu, J. Appl. Phys., 2009, **105**, 054104.

[13] M. Li, A. Feteira, D. C. Sinclair, A. R. West, Appl. Phys. Lett., 2006, **88**, 232903.

[14] Y. B. Qin, H. X. Yang, Y. Zhang, H. F. Tian, C. Ma, L. J. Zeng, J. Q. Li, Appl. Phys. Lett., 2009, **95**, 072901.

[15] J. M. De Teresa, K. Donn, K. H. Muller, L. Schultz, Phys. Rev. B., 1998, **58**, 5928.

[16] J. Benjamin, Sci. Ame., 1976, **234**, 40.

[17] C. Suryanarayana, Prog. Mater. Sci., 2001, **46**, 1.

[18] Ch. Kuhrt, L. Schultz, J. Appl. Phys., 1992, **71**, 1896.

[19] L. Schultz, K. Schnitzke, J. Wecker, J. Appl. Phys., 1988, **64**, 5302.

[20] Che, J. Yao, X. Jian, H. Wang, M. Ceram. Int., 2004, **30**, 1935.

[21] M. Wang, K.D. Woo, C.G. Lee, Energy Conversion and Management, 2011, **52**, 1589.

[22] P. Balaz, M. Achimovicova, M. Balaz, P. Billik, Z. Cherkezova-Zheleva, J. M. Criado, F. Delogu, E. Dutkova, E. Gaffet, F. J. Gotor, R. Kumar, I. Mitov, T. Rojac, M. Senna, A. Streletskii and K. Wieczorek-Ciurowa, Chem. Soc. Rev., 2013, **42**, 7571.

[23] A. Chouket, V. Optasanu, O. Bidault, A. Cheikhrouhou, W. Cheikhrouhou-Koubaa, M. Khitouni, J. All. Com., 2016, **688**, 163.

[24] A. Chouket, W. Cheikhrouhou-Koubaa, A. Cheikhrouhou, V. Optasanu, O. Bidault, M. Khitouni, J. All. Com., 2016, **662**, 467.

[25] A. Chouket, O. Bidault, V. Optasanu, A. Cheikhrouhou, W. Cheikhrouhou-Koubaa, M. Khitouni, RSC. Adv., 2016, **6**, 24543.

[26] L. Lutterotti, Microstructure of Materials, MAUD CPD Newsletter (IUCr), No. 24, 2000.

[27] H. M. Rietveld, J. Appl. Cryst., 1969, **2**, 65.

[28] T. Roisnel, J. Rodriguez-Carvajal, Computer Program FULLPROF, LLB-LCSIM, May 2003.

[29] J. Zhang, R. B. Von Dreele, L. Eyring, J. S. S. Chem., 1996, **122**, 53.

[30] F. G. Correa, J. B. Martinez, Material Science-Poland, 2014, **32**, 682.

[31] M. Sun, B. Lan, T. Lin, G. Cheng, F. Ye, L. Yu, X. Cheng, X. Zheng, Cryst. Eng. Comm., 2013, **15**, 7010.

[32] M. El-Kemary, N. Nagy, I. El-Mehasseb, Materials Science in Semiconductor Processing, 2013, 1**6** (6), 1747.

[33] C. Suryanarayana, Mechanical alloying and milling Progress in Materials Science, 2001, **46**, 1.

[34] A. Taylor, X-ray Metallography, Wiley, New York, 1961.

[35] T. Adams, D. Sinclair, A. West, Physical Review B, 2006, **73**, 094124;

[36] A. West, T. Adams, F. Morrison, D.Sinclair, Journal of the European Ceramic Society, 2004, **24**, 1439.

[37] L. Ni, X. M. Chen, X. D. Liu, R. Z. Hou, Solid State Communications. 2006, **139**, 45.

[38] J. Li, K. Cho, N. Wu, IEEE Transactions on Dielectrics and Electrical Insulation. 2004, **11**, 534.

[39] K. P. Meher, M. Savinov, S. Kamba, V. Goian, K. B. R. Varma, J. Appl. Phys., 2010, **108**, 094108.

[40] E. Iguchi, H. Nakatsugawa, and K. Futakuchi, J. Solid State Chem., 1998, **139**, 176.

[41] A. S. Bondarenko, G. A. Ragoisha, Prog. In Chemometrics Research, 2005, **9** (12), 89.

[42] G. Wu, J. J. Neumeier, Phys. Rev. B., 2003, **67**, 125116.

Table.1. Structural parameters of $PrSrNi_{0.8}Mn_{0.2}O_4$ ceramics milled at different times and sintered at 1300°C for 8 hours resulting from Rietveld refinements of X-ray powder diffraction measurements at room temperature.

Figure captions:

Figure 1: XRD of powders milled at different times (0 h, 5 h, 10 h, 20 h and 30 h), before sintering.

Figure 2: Room temperature X-ray diffraction pattern (measured and calculated) of new observed peaks for (a) 0 h, (b) 5 h (c) 10 h, and (d) 20 h.

Figure 3: Evolutions of the estimated crystallite size and the mean lattice strain of different phases as a function of milling time.

Figure 4: XRD patterns of $PrSrNi_{0.8}Mn_{0.2}O_4$ ceramics milled at different times (5 h; 10 h; 20 h and 30 h) and sintered at 1300 °C in air for 8h. Zoom on the main peak (inset).

Figure 5: Rietveld refinement of the ceramics milled for 30 h and sintered at 1300 °C for 8 hours.

Figure 6: Rietveld refinements of the XRD measurements for the compounds milled at different times: lattice parameters (*a* and *c*) and unit cell volume (*V*).

Figure 7: XPS spectrum for the powder milled for 30 hours.

Figure 8: (a) 2p levels of nickel for 5, 20 and 30 hours of milling. (b) 3d levels of Pr for 5, 20 and 30 hours of milling. (c) 3d levels of Sr for 5, 20 and 30 hours of milling. (d) Evolution of position of 3d levels of Sr between 5 and 30 hours of milling.

Figure 9: FAED pattern along the c axis of the crystal (a); corresponding TEM micrographs (b); HRTEM (c); EDS spectrum (d).

Figure 10: Comparison of dielectric constants and dielectric losses of $PrSrNi_{0.8}Mn_{0.2}O_4$ ceramics at room temperature as a function of the milling time.

Figure 11: Temperature dependences of dielectric characteristics of $PrSrNi_{0.8}Mn_{0.2}O_4$ ceramics at various frequencies for different milling times: 5 h, 10 h and 30 h.

Figure 12: Frequency dependence of dielectric constants at low temperatures for $PrSrNi_{0.8}Mn_{0.2}O_4$ milled for different times (left). The solid lines are the polydispersion Debye

fittings. Relaxation time as a function of 1000/T (right). The solid lines are the Arrhenius fittings.

Figure 13: Complex impedance spectra of the ceramics at various temperatures (measured and fitted with [R-C][R-CPE]). Corresponding bulk / grain boundary resistances and fitting with the adiabatic small polaronic hoppings.

Table 1

	Milling times			
Parameter	***5 h***	***10 h***	***20 h***	***30 h***
a (Å)	3.8065(7)	3.8011(3)	3.8011(8)	3.8031(8)
c (Å)	12.4029(2)	12.4709(2)	12.4724(4)	12.4764(4)
Volume ($Å^3$)	179.711	180.184	180.205	180.453
$\chi 2$	1.58	1.41	1.40	1.42
Rp (%)/Rwp(%)	2.78/5.41	2.83/5.63	3.13/4.72	2.24/4.69
D_{sc}(nm)	76.06	68.87	61.01	52.88

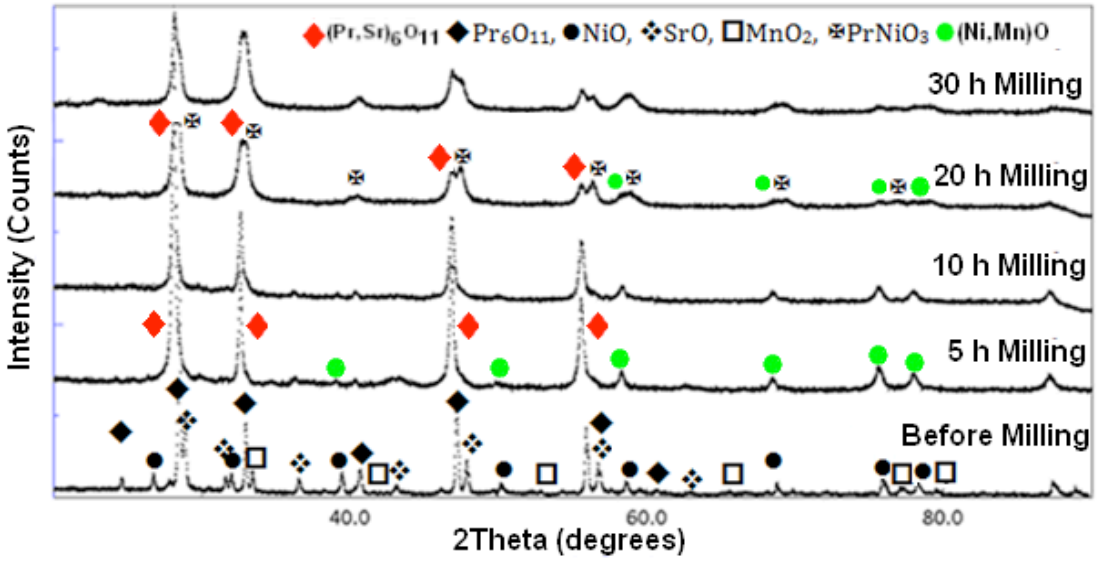

Figure 1

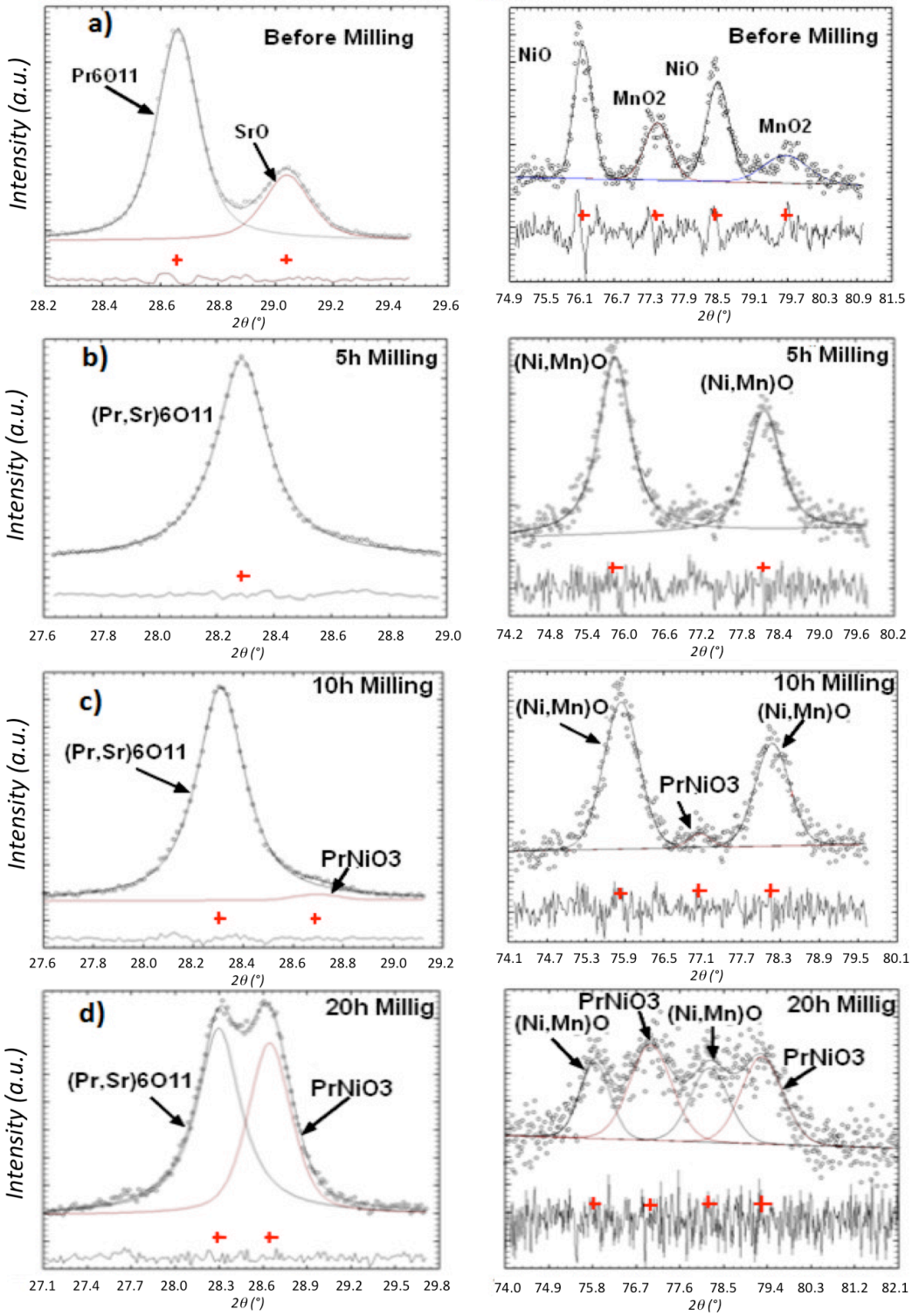
a)
Before Milling
Pr6O11
SrO
Intensity (a.u.)
28.2 28.4 28.6 28.8 29.0 29.2 29.4 29.6
2θ (°)
Before Milling
NiO
NiO
MnO2
MnO2
74.9 75.5 76.1 76.7 77.3 77.9 78.5 79.1 79.7 80.3 80.9 81.5
2θ (°)
b)
5h Milling
(Pr,Sr)6O11
Intensity (a.u.)
27.6 27.8 28.0 28.2 28.4 28.6 28.8 29.0
2θ (°)
5h Milling
(Ni,Mn)O
(Ni,Mn)O
74.2 74.8 75.4 76.0 76.6 77.2 77.8 78.4 79.0 79.6 80.2
2θ (°)
c)
10h Milling
(Pr,Sr)6O11
PrNiO3
Intensity (a.u.)
27.6 27.8 28.0 28.2 28.4 28.6 28.8 29.0 29.2
2θ (°)
10h Milling
(Ni,Mn)O
(Ni,Mn)O
PrNiO3
74.1 74.7 75.3 75.9 76.5 77.1 77.7 78.3 78.9 79.5 80.1
2θ (°)
d)
20h Millig
(Pr,Sr)6O11
PrNiO3
Intensity (a.u.)
27.1 27.4 27.7 28.0 28.3 28.6 28.9 29.2 29.5 29.8
2θ (°)
PrNiO3
(Ni,Mn)O
(Ni,Mn)O
20h Millig
PrNiO3
74.0 74.9 75.8 76.7 77.6 78.5 79.4 80.3 81.2 82.1
2θ (°)

Figure 2

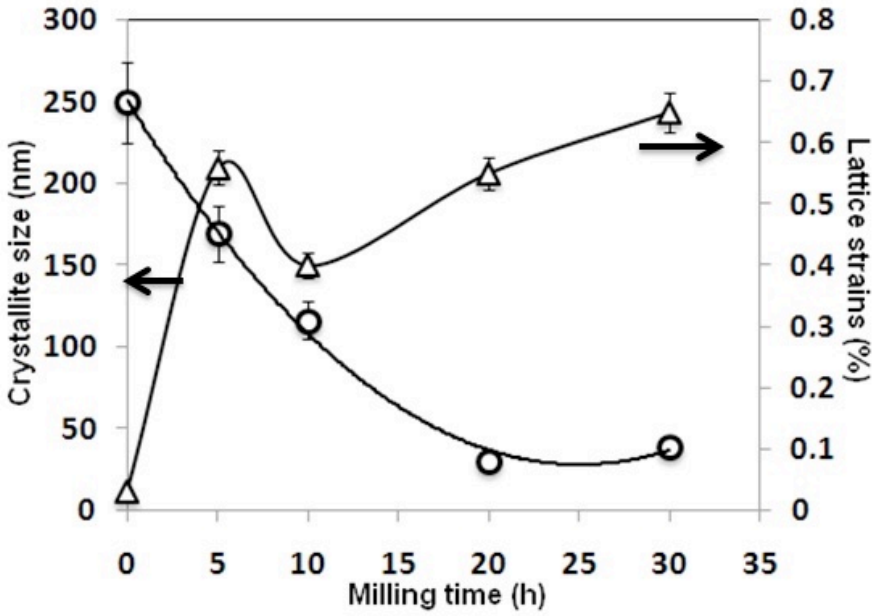
Crystallite size (nm)
Lattice strains (%)
Milling time (h)
300
250
200
150
100
50
0
0.8
0.7
0.6
0.5
0.4
0.3
0.2
0.1
0
0
5
10
15
20
25
30
35

Figure 3

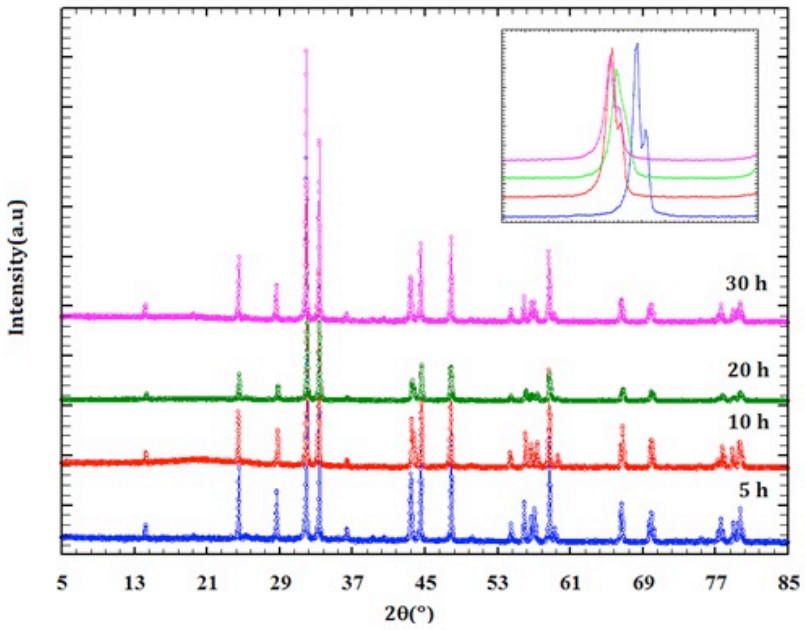

Figure 4

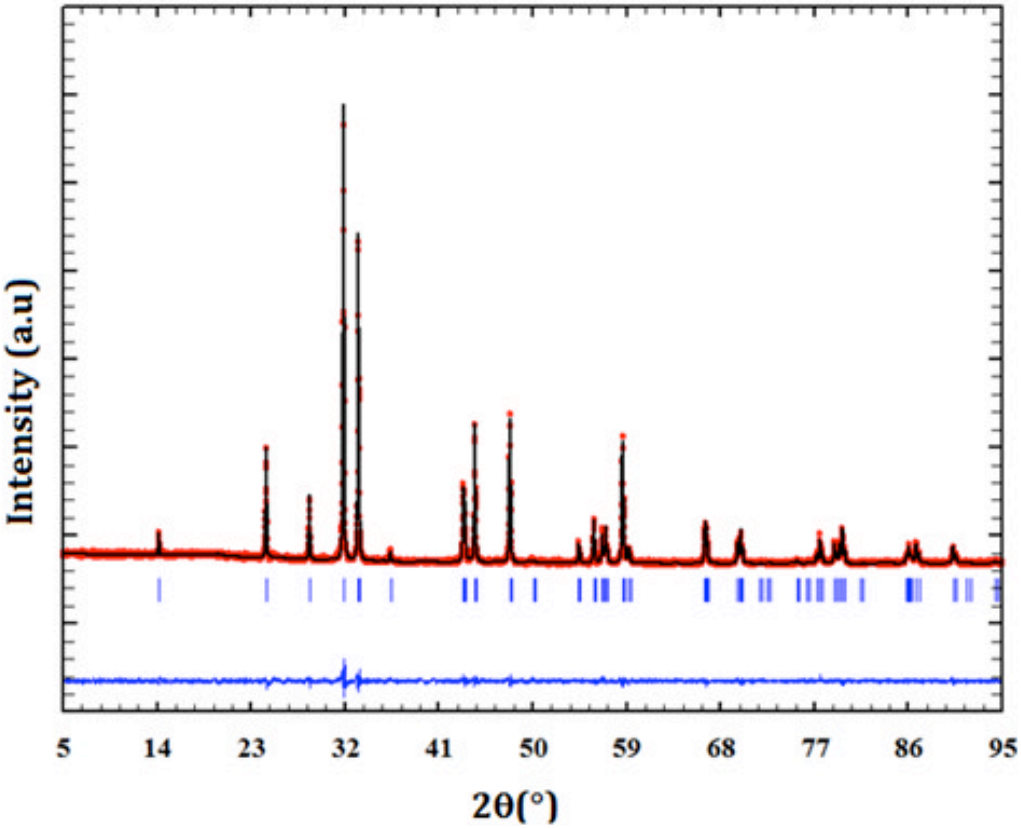

Figure 5

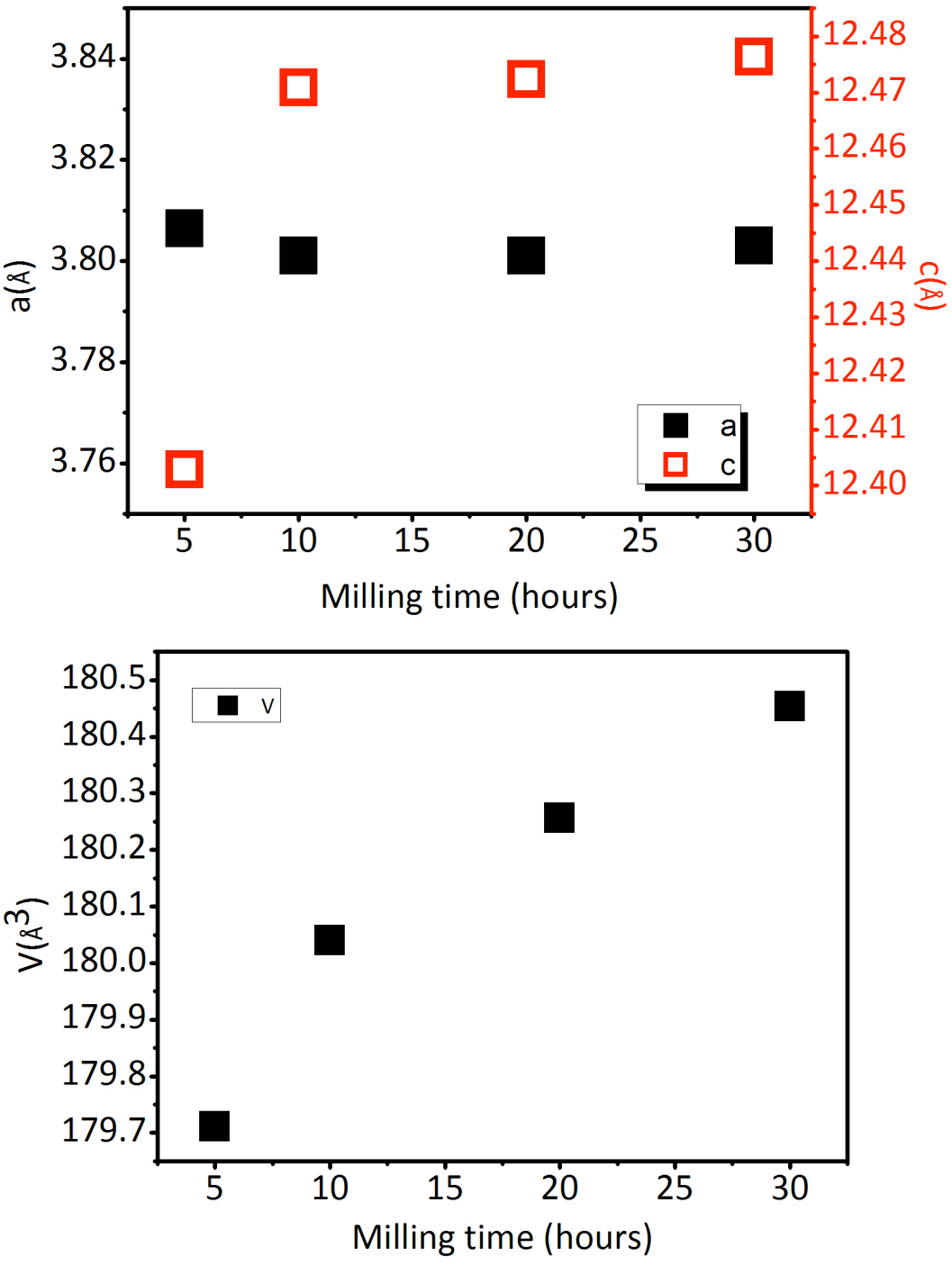
3.84
3.82
3.80
3.78
3.76
a(Å)
12.48
12.47
12.46
12.45
12.44
12.43
12.42
12.41
12.40
c(Å)
a
c
5
10
15
20
25
30
Milling time (hours)
180.5
180.4
180.3
180.2
180.1
180.0
179.9
179.8
179.7
V(Å3)
V
5
10
15
20
25
30
Milling time (hours)

Figure 6

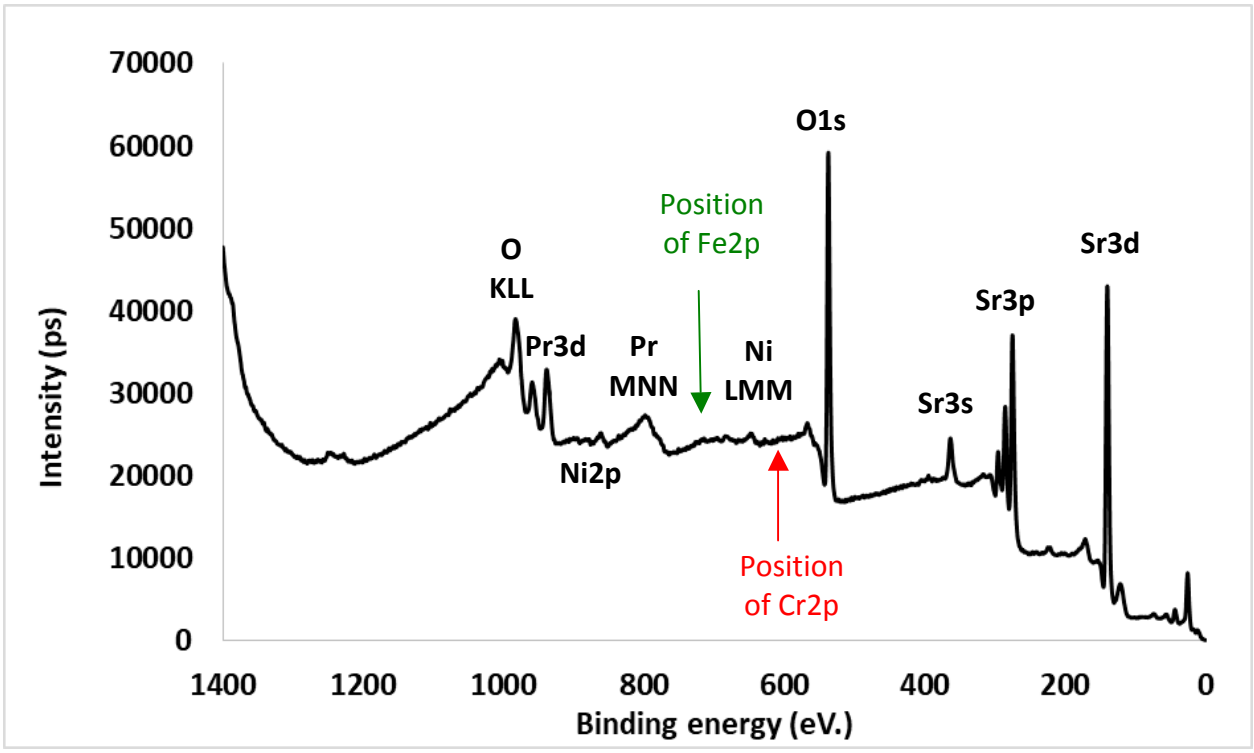
70000
60000
50000
40000
30000
20000
10000
0
Intensity (ps)
1400
1200
1000
800
600
400
200
0
Binding energy (eV.)
O
KLL
Pr3d
Ni2p
Pr
MNN
Position
of Fe2p
Ni
LMM
O1s
Position
of Cr2p
Sr3s
Sr3p
Sr3d

Figure 7

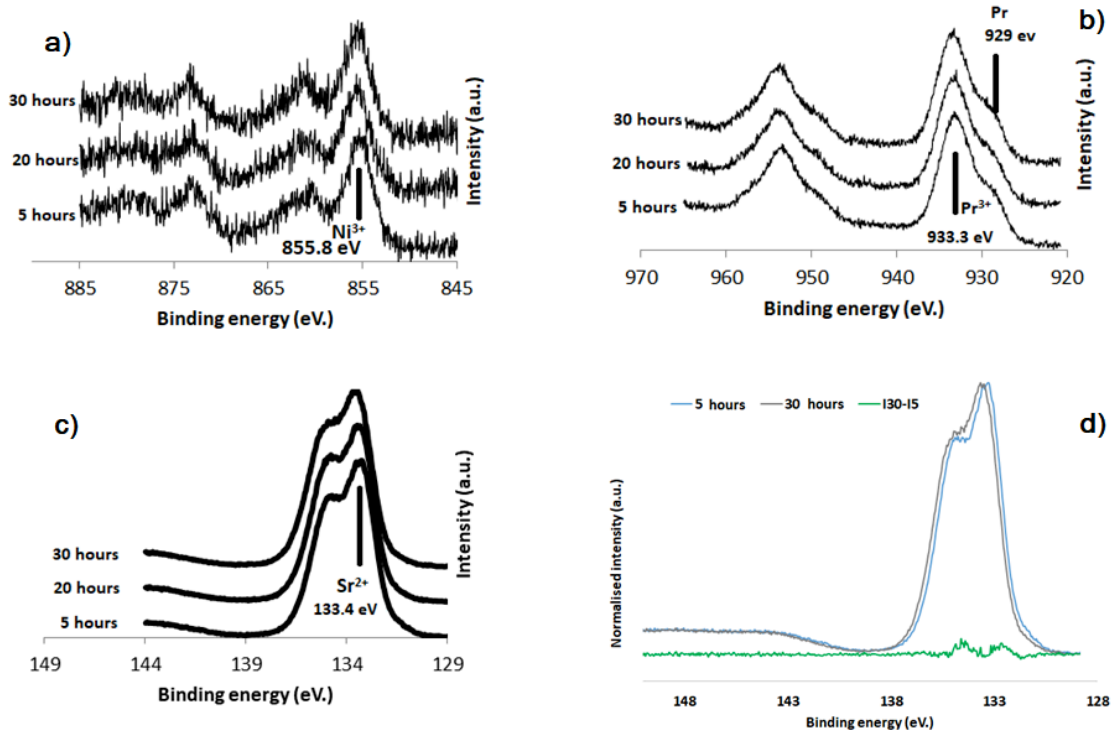
a)
30 hours
20 hours
5 hours
Ni3+
855.8 eV
Intensity (a.u.)
885
875
865
855
845
Binding energy (eV.)
b)
Pr
929 ev
30 hours
20 hours
5 hours
Pr3+
933.3 eV
Intensity (a.u.)
970
960
950
940
930
920
Binding energy (eV.)
c)
30 hours
20 hours
5 hours
Sr2+
133.4 eV
Intensity (a.u.)
149
144
139
134
129
Binding energy (eV.)
d)
5 hours
30 hours
I30-I5
Normalised intensity (a.u.)
148
143
138
133
128
Binding energy (eV.)

Figure 8

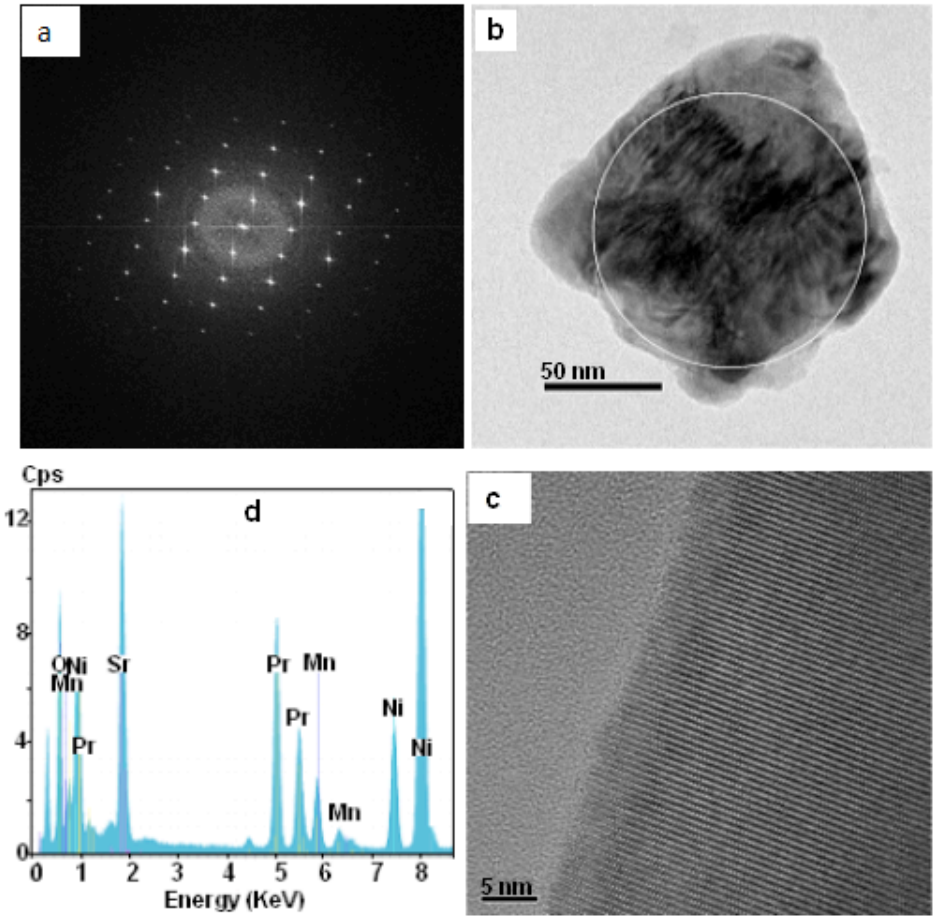
a
b
50 nm
Cps
d
12
8
4
0
O
Ni
Mn
Sr
Pr
Mn
Pr
Ni
Ni
Pr
Mn
0 1 2 3 4 5 6 7 8
Energy (KeV)
c
5 nm

Figure 9

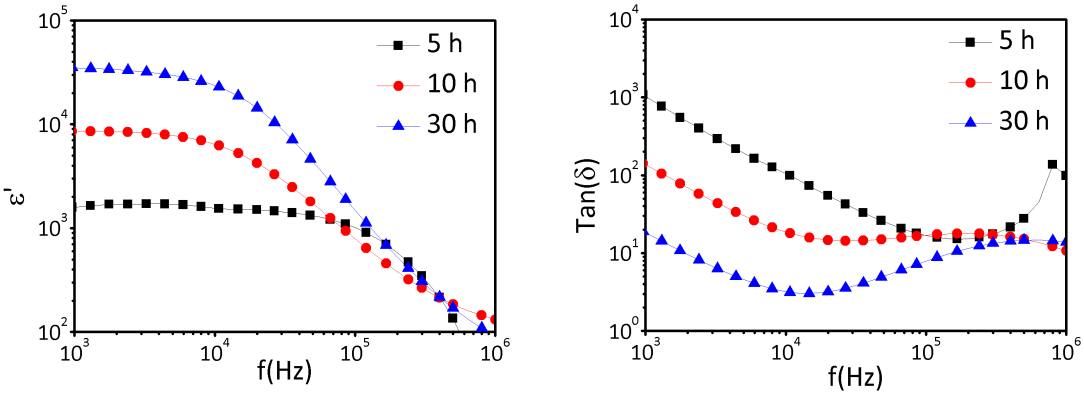

Figure 10

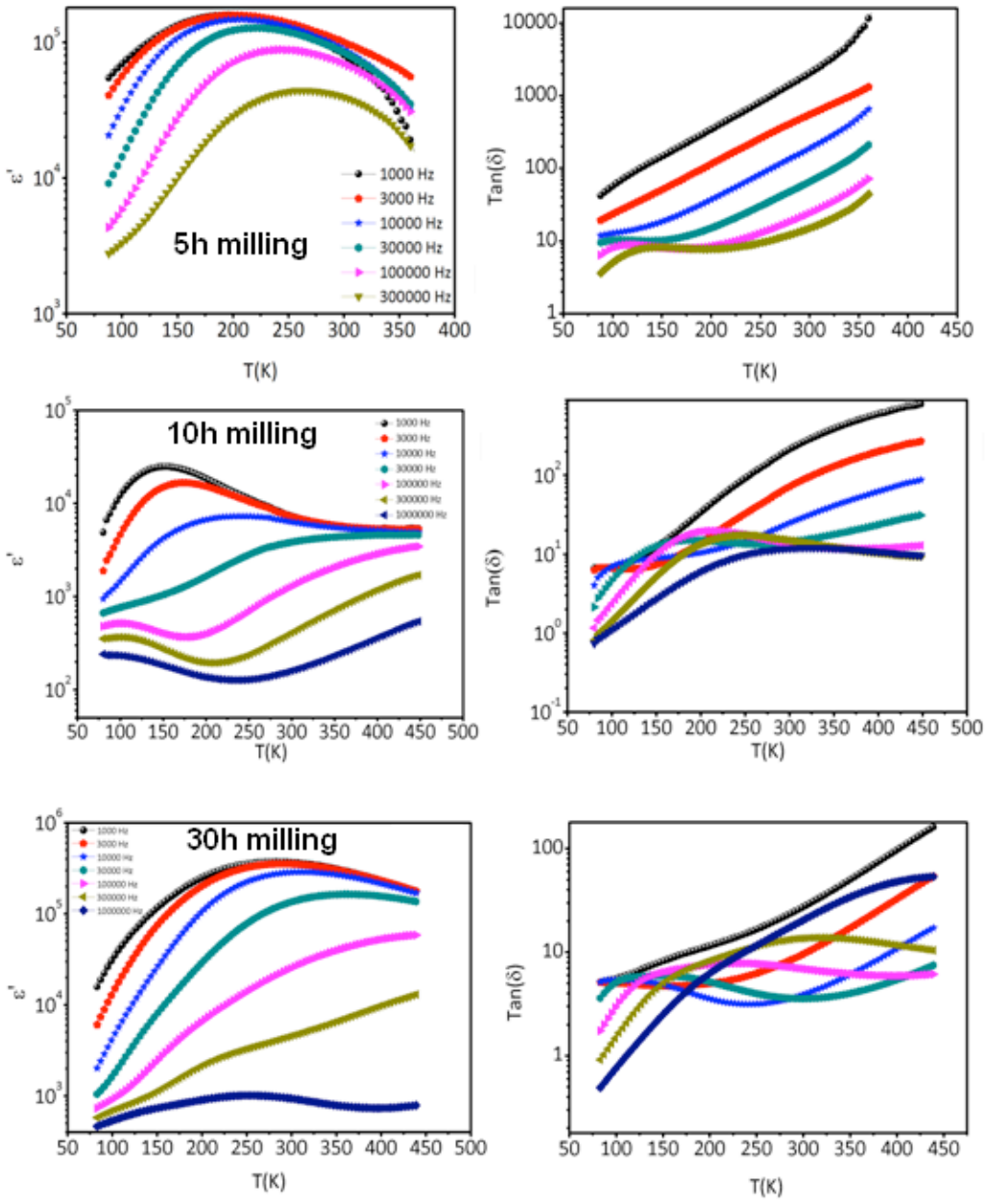
5h milling
1000 Hz
3000 Hz
10000 Hz
30000 Hz
100000 Hz
300000 Hz
ε'
Tan(δ)
T(K)
10h milling
30h milling

Figure 11

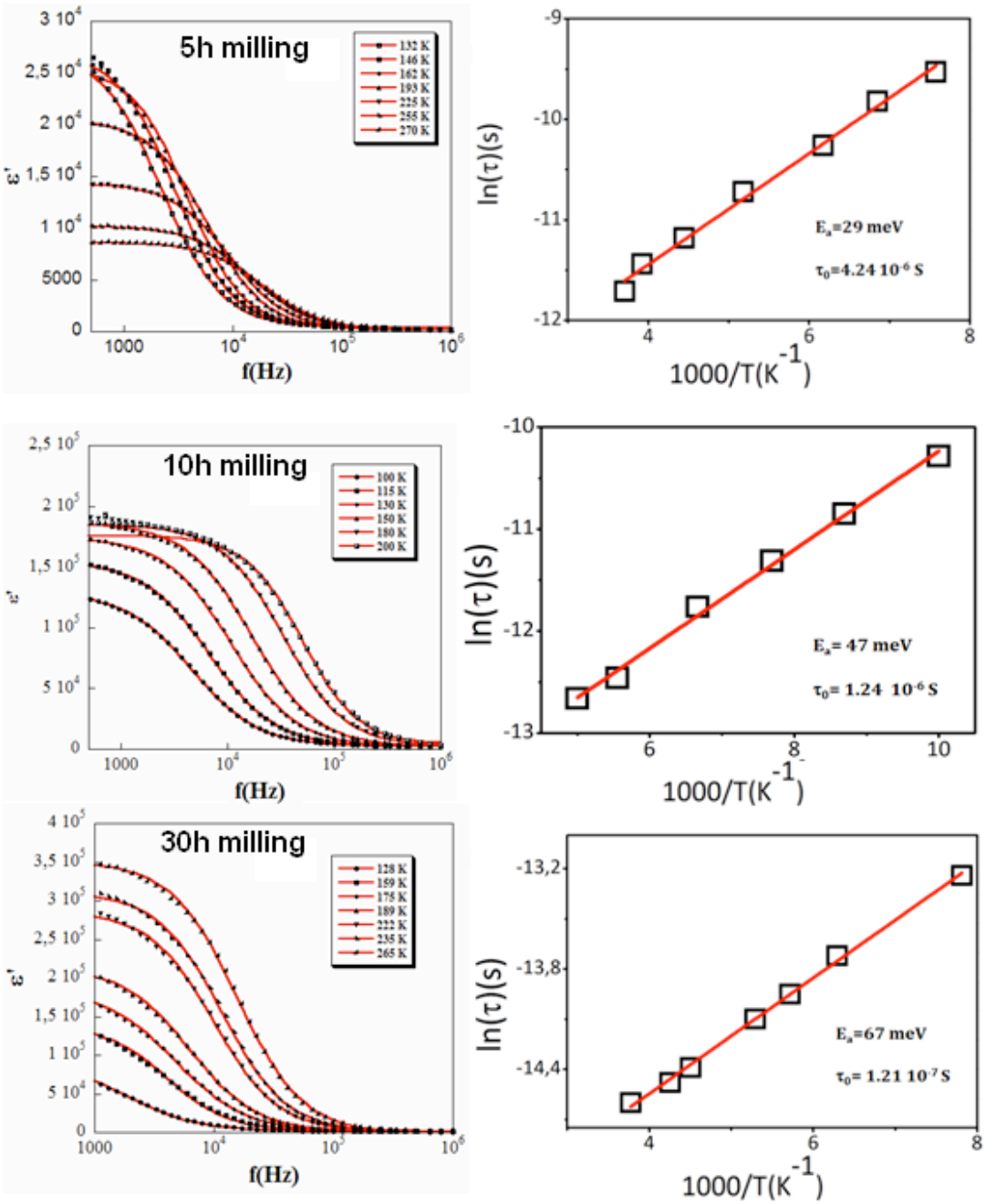
5h milling
132 K
146 K
162 K
193 K
225 K
255 K
270 K
ε'
f(Hz)
ln(τ)(s)
E_a=29 meV
τ_0=4.24 10^-6 S
1000/T(K^-1)
10h milling
100 K
115 K
130 K
150 K
180 K
200 K
ε'
f(Hz)
ln(τ)(s)
E_a= 47 meV
τ_0= 1.24 10^-6 S
1000/T(K^-1)
30h milling
128 K
159 K
175 K
189 K
222 K
235 K
265 K
ε'
f(Hz)
ln(τ)(s)
E_a=67 meV
τ_0= 1.21 10^-7 S
1000/T(K^-1)

Figure 12

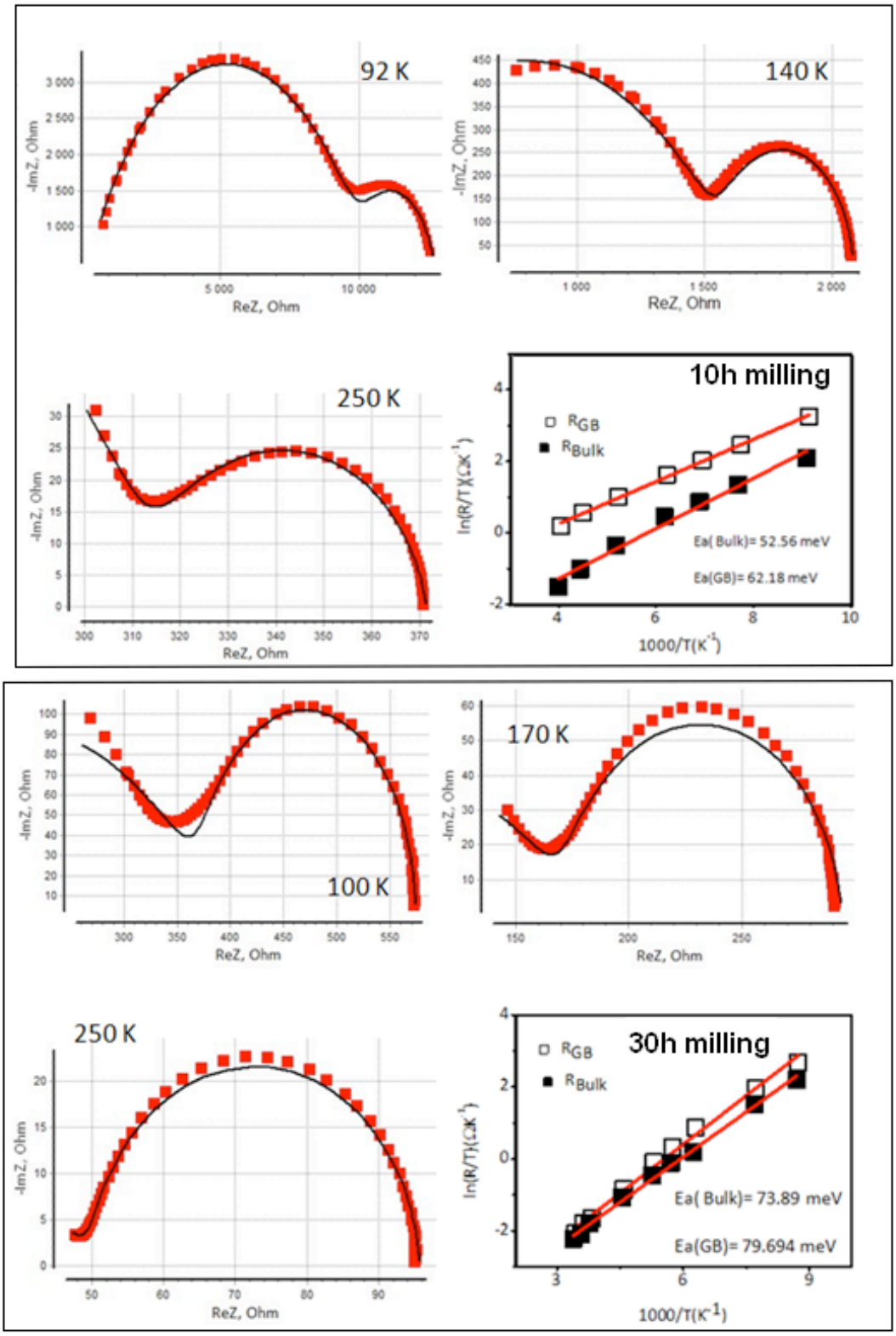
92 K
140 K
250 K
10h milling
100 K
170 K
250 K
30h milling
-ImZ, Ohm
ReZ, Ohm
R_GB
R_Bulk
Ea(Bulk)= 52.56 meV
Ea(GB)= 62.18 meV
Ea(Bulk)= 73.89 meV
Ea(GB)= 79.694 meV
1000/T(K^-1)

Figure 13